Wideband signal detection based on high-speed photonic analog-to-digital converter

Guang Yang (杨 光), Weiwen Zou (邹卫文)*, Ye Yuan (袁 野), and Jianping Chen (陈建平)

State Key Laboratory of Advanced Optical Communication Systems and Networks, Department of Electronic Engineering, Shanghai Jiao Tong University, Shanghai 200240, China

**Corresponding author: wzou@sjtu.edu.cn*

Received September 26, 2017; accepted December 1, 2017; posted online March 6, 2018

This Letter demonstrates the effectiveness of a high-speed high-resolution photonic analog-to-digital converter (PADC) for wideband signal detection. The PADC system is seeded by a high-speed actively mode locked laser, and the sampling rate is multiplied via a time-wavelength interleaving scheme. According to the laboratory test, an X-band linear frequency modulation signal is detected and digitized by the PADC system. The channel mismatch effect in wideband signal detection is compensated via an algorithm based on a short-time Fourier transform. Consequently, the signal-to-distortion ratio (SDR) of the wideband signal detection is enhanced to the comparable SDR of the single-tone signal detection.

OCIS codes: 060.5625, 230.0250, 250.4745, 000.4430.
doi: 10.3788/COL201816.030601.

In modern radar systems, wideband signals are extensively used to achieve a high resolution of the target detection. However, the wide bandwidth brings big challenges for analog-to-digital converters (ADCs) in the reception of signals[1]. The state-of-the-art electronic ADCs provide an instantaneous bandwidth of ~2 GHz and a timing accuracy of ~100 fs[2,3]. Further improvement is limited by the timing accuracy and analog bandwidth. Fortunately, the photonic ADC (PADC) has been proposed to break the limitation of electronic ADCs[4,5]. In the PADC systems, the ultra-stable mode-locked lasers (MLLs) are used to generate sampling clocks with low timing jitters, and the photonic-modulator-based sampling gates enlarge the bandwidth of the analog input effectively[6]. Juodawlkis *et al.* presented a 60 MS/s down-sampling of an X-band linear frequency modulation (LFM) signal[7]. Ghelfi *et al.* demonstrated the reception of X-band and Kα-band LFM signals via a 400 MS/s down-sampling in a coherent photonic radar, providing a resolution of 150 m in distance and 2 km/h in velocity in the X-band[8]. However, due to the low repetition rate of the passively MLL (PMLL), the effective sampling rate of the PADC is limited to be low, which cannot fully exploit the large spectral range of the high-frequency carrier. It is worth mentioning that the time-stretched PADC scheme is an effective method to achieve an ultrahigh equivalent sampling rate by use of a low-repetition-rate MLL source[9,10]. Most recently, we implemented a photonic transceiver for wideband radar based on the time-stretched PADC scheme[11]. However, these schemes suffer from the limited-time aperture in the single-shot mode[9]. Moreover, with verified effectiveness in the applications, such as spectrum sensing and radar imaging[12,13], the photonic processing of the wideband signal is drawing more and more attention in related fields.

In order to further enhance the sampling rate for a larger input bandwidth, we have demonstrated the generation of a high-speed sampling clock and a high-speed time-wavelength interleaving PADC (TWI-PADC) system based on an actively MLL (AMLL)[14–16]. So far, the methods used for resolution evaluation and mismatch compensation in the high-speed TWI-PADC system are only verified with the single-tone input signal. To meet the requirements in a practical radar system, these methods should be further tested with wideband input signals, especially the LFM signals that are the most commonly used radar waveform.

In this Letter, a wideband LFM signal with a frequency range of 8–12 GHz is detected and then digitized by an AMLL-based TWI-PADC with a 40 GS/s sampling rate. Since the signal reception in TWI-PADC always suffers from channel mismatch induced distortion, a theoretical model of signal-to-distortion ratio (SDR) for a wideband LFM signal is derived to evaluate the channel mismatch effects based on the short-time Fourier transform (STFT) of the digitized data. Consequently, the SDR of the digitization data is enhanced from 37 to 52 dB after hardware adjustment and algorithmic compensation.

The experimental configuration of the TWI-PADC system is illustrated in Fig. 1(a). An AMLL (Calmar PSL-10-TT) seeded by an electronic synthesizer (Keysight E8257D) at 10 GHz serves as the laser source. After being spectrally broadened by a pulse compressor (Calmar PCS-2), its output is multiplexed by a four-channel TWI multiplexer (TWI-MUX), so as to four-fold enhance the photonic sampling clock (from 10 to 40 GHz)[14]. Limited by the optical spectral bandwidth of the AMLL and pulse compressor, to guarantee the optical powers in each channel, the number of channels is difficult to be further added. However, thanks to the high repetition rate of the

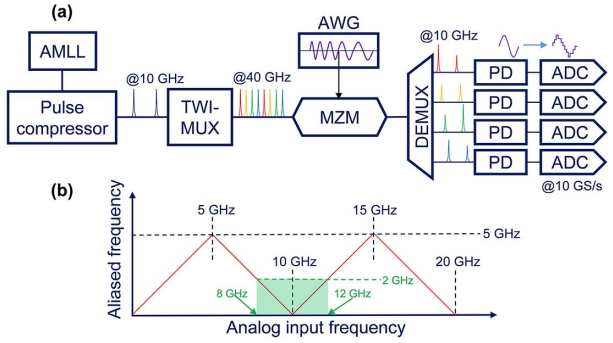

Fig. 1. (a) Experimental configuration of photonic analog-to-digital conversion for X-band wideband signal detection. (b) Schematic of the relation between the wideband input signal and the aliased frequency in each channel. AMLL, actively mode locked laser; TWI-MUX, time-wavelength interleaving multiplexer; MZM, Mach–Zehnder modulator; DEMUX, demultiplexer; AWG, arbitrary waveform generator; PD, photodetector; ADC, analog-to-digital converter.

AMLL, the high sampling rate of 40 GS/s is realized by four channels, and a lower-complexity configuration is maintained if compared with the PMLL-based PADC system[7,8]. In Ref. [15], the feasibility of the TWI-MUX-based configuration for the single-tone signal with 40 GS/s sampling rate has been demonstrated. In order to verify the ability of the wideband signal detection, an LFM signal is generated by an arbitrary waveform generator (AWG, Keysight M8195A) working with the digital-to-analog conversion rate of 64 GS/s. The photonic sampling gate is implemented by modulating the LFM signal on the photonic sampling clock via a Mach–Zehnder modulator (MZM, Photoline MXIQ-LN-40) with an input radio frequency (RF) bandwidth of 40 GHz. The photonic sampled signal is divided into four parallel channels by a wavelength demultiplexer (DEMUX). The parallelized photonic signal is converted into the electronic signal via a photodetector (PD, Discovery DSC-R401HG-59) array and then digitized by a four-channel real-time oscilloscope (Keysight MSOS804A) with the sampling rate of 10 GS/s and analog bandwidth of ~4.2 GHz for each channel. Figure 1(b) depicts the relation between the analog input frequency and aliased frequency in one channel. It indicates that an X-band signal with the frequency range of 8–12 GHz is aliased within a 2 GHz bandwidth in each channel.

The LFM signal to be sampled is expressed by

$$v_{\mathrm{IN}}(t) = V_0 \mathrm{rect}\left\{\frac{t}{T}\right\} \sin(2\pi f_0 t + \pi K t^2), \qquad (1)$$

where V_0 is the amplitude of the LFM signal, rect$\{\cdot\}$ is the rectangular pulse envelope, T is the duration of the LFM envelope pulse, f_0 is the start frequency, and K is the LFM chirp rate. The frequency sweeping range is set to be 8–12 GHz, and the parameters of the LFM signal are set to be $T = 1$ μs, $f_0 = 8$ GHz, and $K = 4 \times 10^6$ GHz/s. The amplitude is manipulated according to the optimization of modulation index[16]. Simulated results of the X-band LFM signal are illustrated in Fig. 2. The temporal waveform of the generated LFM signal is depicted in Fig. 2(a), and its STFT spectrum is given in Fig. 2(b).

The wideband signal detection is characterized in the frequency domain. The input and output microwave response of the PADC system is measured and illustrated in Fig. 3(a). All of these responses are measured via a network analyzer (Agilent PNA-X N5245A) and an RF spectral analyzer (R&S FSUP 50). The input microwave response is determined by the output response of the AWG, and the output microwave response is decided by the cascaded response of the MZM, PD, and oscilloscope. It indicates the capability of the PADC in the detection of the wideband LFM signal shown in Fig. 2. In Fig. 3(b), a comparison between the fast Fourier transform (FFT) spectra of the digitized data and the theoretical simulation is depicted. It is found that there are slight fluctuations in magnitude induced by the non-uniformity of the microwave response [see Fig. 3(a)]. Moreover, it should be noted that there are two spectral notches at the frequencies of 5 and 15 GHz, which are induced by the limited bandwidth of the oscilloscope used in this study.

Based on the theory in Ref. [15], the channel mismatch induced distortions of the 8–12 GHz LFM signal should be located in the frequency range of 0–2 GHz, 8–12 GHz, and 18–20 GHz, respectively. From the spectral comparison in Fig. 3(b), one can find that the channel mismatch induced distortions at 0–2 GHz and 18–20 GHz are distinguished. However, the mismatch distortions at 8–12 GHz are

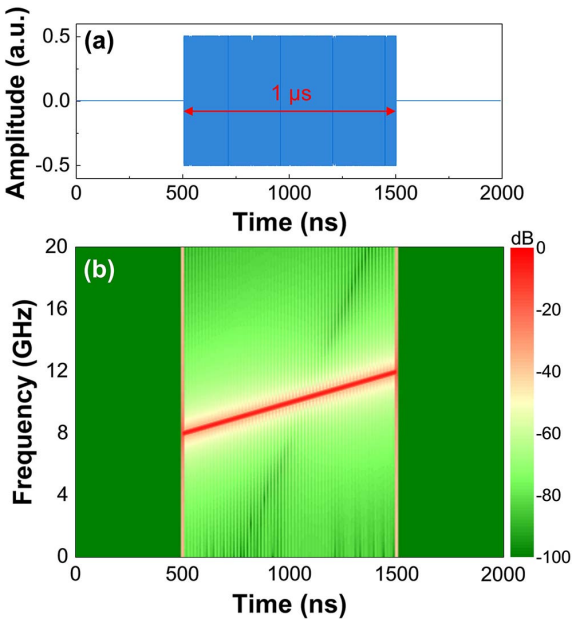

Fig. 2. Simulated results of the X-band linear frequency modulation signal. (a) Temporal waveform. (b) Normalized short-time Fourier transform of the waveform in (a).

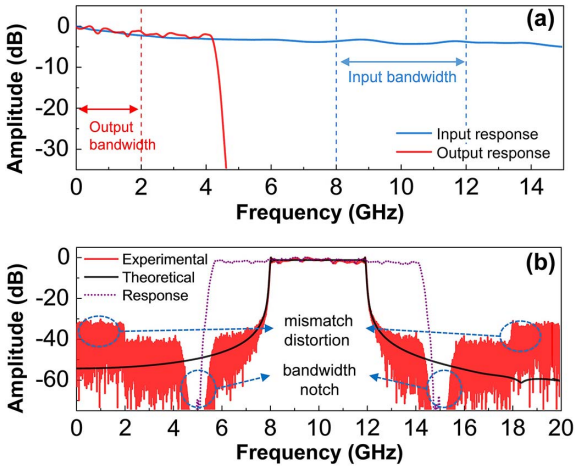

Fig. 3. (a) Normalized input and output microwave response of the PADC system. (b) Normalized FFT spectrum of the digitized data compared with the theoretical simulation and the effective microwave response.

overlapped with the signal in the FFT spectrum, which brings in an obstacle toward the spectral analysis for resolution evaluation. Considering the characteristics of the LFM signal, the STFT could provide its instantaneous spectrum changing with time, which can be considered as a series of spectra of single-tone signals at different frequencies[17]. Hence, the STFT together with the channel mismatch compensation algorithm proposed in Ref. [15] is possible for developing a compensation algorithm for the detection of the wideband LFM signal.

The working principle of this compensation algorithm is illustrated in Fig. 4. First, the data in each channel is interleaved in sequence. Second, the interleaved data is transformed into the STFT spectrum $S[f,t]$ with $0<f<f_s/2$, where f_s is the sampling rate. Meanwhile, the data in each channel is also transformed into the STFT spectrum $(S_n[f,t])$, where $0<f<f_s/(2N)$, and N is the number of channels. At a specific time of τ, the STFT spectrum $S[f,\tau]$ can be regarded as an FFT spectrum of a single-tone signal with the instantaneous frequency of $f_{\mathrm{IN}}(\tau)$. Third, according to the compensation algorithm for the single-tone signal demonstrated in Ref. [15], the channel mismatches of the amplitude (a_n) and time skew (Δt_n) in the nth channel $(n=1,2,...,N)$ can be extracted from the spectral peaks on $S[f,\tau]$ as follows:

$$a_n=\left|\sum_{k=1}^{N}P_k e^{j\frac{2\pi(k-1)(n-1)}{N}}\right|,\quad \Delta t_n=\frac{1}{f_{\mathrm{IN}}}\arg\left[\sum_{k=1}^{N}P_k e^{j\frac{2\pi(k-1)(n-1)}{N}}\right], \tag{2}$$

where $f_{\mathrm{IN}}=f_{\mathrm{IN}}(\tau)$ and P_k represents the complex spectral peak value at the frequency of $f=(k-1)f_s/N\pm f_{\mathrm{IN}}$. Consequently, the STFT spectrum in each channel can be compensated in both amplitude and timing, which is given by

$$S_n^*[f,t]=\frac{\bar{a}}{a_n}e^{-j2\pi f_{\mathrm{IN}}(t)\Delta t_n}S_n[f,t],\quad n=1,2,\cdots,N, \tag{3}$$

where $\bar{a}$ is the mean value of the amplitudes in all channels. Eq. (3) shows that the STFT spectrum $S_n[f,t]$ is compensated into $S_n^*[f,t]$. After the STFT spectrum in each channel is compensated, the digitized data can be achieved by an inverse STFT[17] and reconstructed via the channel interleaving.

The normalized STFT spectra of the X-band LFM signal before and after channel mismatch compensation are compared in Figs. 5(a) and 5(b). The compensation algorithm given in Eq. (3) is applied to the profiles of the original STFT spectrum after the channel mismatches defined in Eq. (2) are evaluated for one specific frequency.

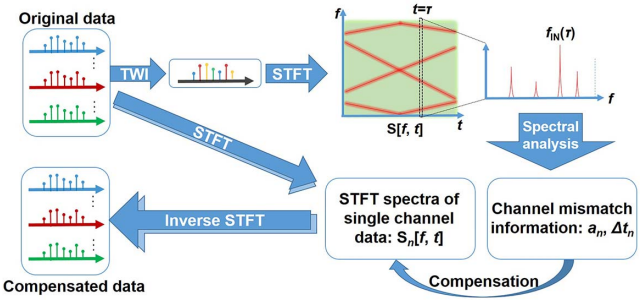

Fig. 4. Working principle of the channel mismatch compensation algorithm for the wideband signal. TWI, time-wavelength interleaving; STFT, short-time Fourier transform.

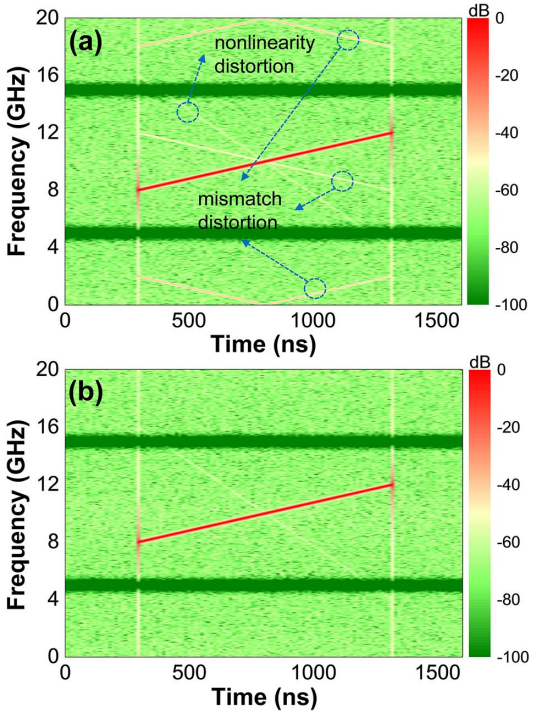

Fig. 5. Experimental results. Normalized STFT spectra of the digitized LFM signal (a) before and (b) after mismatch compensation.

After the compensation algorithm is applied to Fig. 5(a), the channel mismatch distortions are effectively eliminated, as shown in Fig. 5(b). From Fig. 5, it can be found that two spectral notches appear at the same positions (5 and 15 GHz), as shown in Fig. 3(b). Although the noise floor in the STFT is ~ -60 dB, the amplitude in the notches reaches below -80 dB due to the steep cutoff of the input response of the oscilloscope. Two instantaneous STFT spectra at the instantaneous frequencies of 9 and 11 GHz are plotted in Figs. 6(a) and 6(b), respectively. It can be found that the instantaneous STFT spectra of the LFM signal are similar to the spectra of single-tone signals. The comparison before and after the compensation is also depicted in Fig. 6. One can find that the mismatch distortions (i.e., 1, 11, 19 GHz at 9 GHz and 1, 9, 19 GHz at 11 GHz) are effectively eliminated. However, there is still the residual distortion (i.e. 13 GHz at 9 GHz and 7 GHz at 11 GHz), which is induced by the nonlinearity of the MZM. By use of a dual-output MZM[16], the nonlinearity of the MZM for the wideband signal detection is possibly eliminated.

In principle, the resolution of the PADC system should be evaluated via the signal-to-noise-and-distortion ratio (SINAD), which is a combination of the signal-to-noise ratio (SNR) and the SDR. In Ref. [15], the SNR and SDR in the PADC induced by both photonic and electronic components were analyzed and modeled. However, the AWG that generates the wideband signal has a noise level higher than that of the PADC system[18], which dominates both the photonic and electronic noise in the PADC system[15]. Hence, the SNR is inappropriate to evaluate the resolution of the PADC system for wideband signal detection. Here, we characterize the wideband signal detection in term of the SDR. The SDR in PADC for single-tone input can be expressed as[15]

$$\mathrm{SDR}[f] = -20\log\sqrt{4\pi^2 f^2\sigma_t^2 + \sigma_a^2 + \delta_M^2}, \tag{4}$$

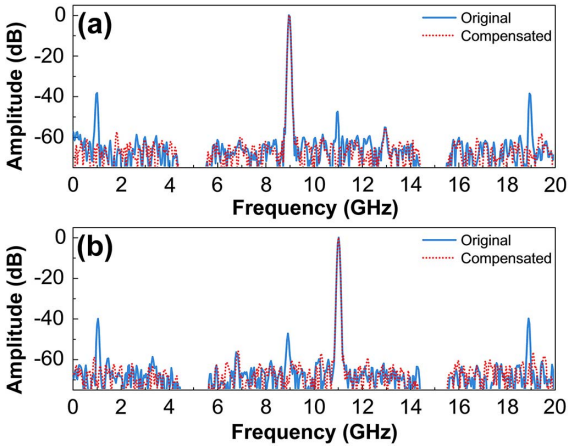

Fig. 6. Comparison between the instantaneous STFT spectra before and after channel mismatch compensation at the instantaneous frequencies of (a) 9 GHz and (b) 11 GHz.

where f is the input frequency, and σ_a and σ_t are the standard deviation of amplitude and time skew in each channel, respectively. δ_M denotes the distortion induced by the modulation nonlinearity. Referred to Eq. (4), the SDR for the LFM signal can be calculated by

$$\mathrm{SDR}_{\mathrm{LFM}} = -20\log\left(\sum_f S[f]10^{-\frac{\mathrm{SDR}[f]}{10}}/\sum_f S[f]\right), \tag{5}$$

where $S[f]$ is the power of the STFT spectrum at f, and the summation is carried out in the sweeping bandwidth of the LFM signal.

The characterized SDR for different channel mismatches is depicted in Fig. 7. The experimental values are calculated from the STFT spectra and compared with the theoretical estimation according to Eqs. (2) and (3). Figure 7(a) illustrates the channel match accuracy, where the contours denote the theoretical estimation. The hardware adjustments are optimized by tuning the delays and amplitudes in each channel of the TWI-MUX, as shown in Ref. [15]. The channel mismatch compensation algorithm is employed after the hardware optimization. Figure 7(a) shows that the SDR is first enhanced by the hardware adjustment and then by the algorithmic compensation.

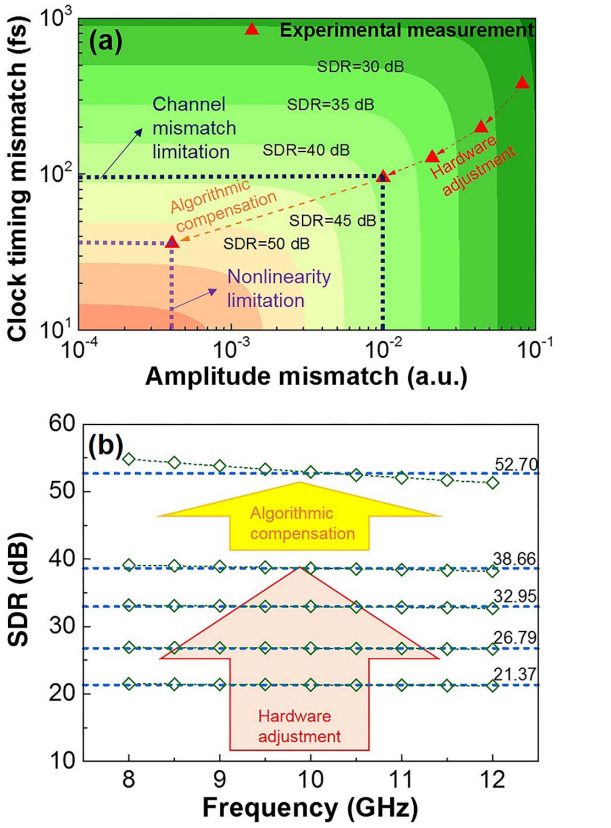

Fig. 7. Characterized signal-to-distortion ratio (SDR) for different channel mismatches. (a) Channel mismatches after hardware adjustments and algorithmic compensation. (b) SDR measured from STFT spectra (dashed curve) and from the instantaneous spectrum at one specific frequency (dotted curve with symbols) after each step adjustment.

According to Eq. (5), the SDR of the STFT spectra for both the LFM signal and single-tone signal at one specific frequency in the sweeping range are evaluated. From Fig. 7(b), it can be found that SDR increases from 21 to 37 dB after the hardware adjustments and is further enhanced from 37 to 52 dB after the channel mismatch compensation. Note that the SDR of the LFM signal is well consistent with that of the equivalent single-tone signal.

In conclusion, we have demonstrated the digitization of an X-band LFM signal with the frequency range of 8–12 GHz via a four-channel 40 GS/s AMLL based TWI-PADC. With the STFT, the compensation algorithm of the TWI-PADC that was adapted for the single-tone signal detection can be effectively applied to the wideband signal detection. The SDR for the wideband signal detection is derived and evaluated to be ∼52 dB. It is verified that the TWI-PADC is feasible for detecting the wideband signal with good performance (i.e., the sampling rate of 40 GS/s, the instantaneous bandwidth of 4 GHz at the X-band, and the SDR of ∼52 dB), which may find potential applications for wideband radar reception.

This work was partially supported by the National Natural Science Foundation of China (Nos. 61571292 and 61535006).

References

1. J. A. Wepman, IEEE Commun. Mag. **33**, 39 (1995).
2. R. H. Walden, "Analog-to-digital conversion in the early 21st century," in *Wiley Encyclopedia of Computer Science and Engineering* (Wiley, 2007), p. 1.
3. B. Murmann, "ADC performance survey 1997–2017," http://web.stanford.edu/~murmann/adcsurvey.html (2017).
4. G. C. Valley, Opt. Express **15**, 1955 (2007).
5. A. Khilo, S. J. Spector, M. E. Grein, A. H. Nejadmalayeri, C. W. Holzwarth, M. Y. Sander, M. S. Dahlem, M. Y. Peng, M. W. Geis, N. A. DiLello, J. U. Yoon, A. Motamedi, J. S. Orcutt, J. P. Wang, C. M. Sorace-Agaskar, M.A. Popović, J. Sun, G. R. Zhou, H. Byun, J. Chen, J. L. Hoyt, H. I. Smith, R. J. Ram, M. Perrott, T. M. Lyszczarz, E. P. Ippen, and F. X. Kärtner, Opt. Express **20**, 4454 (2012).
6. J. Kim, M. J. Park, M. H. Perrott, and F. X. Kärtner, Opt. Express **16**, 16509 (2008).
7. P. W. Juodawlkis, J. J. Hargreaves, R. D. Younger, G. W. Titi, and J. C. Twichell, J. Lightwave Technol. **21**, 3116 (2003).
8. P. Ghelfi, F. Laghezza, F. Scotti, G. Serafino, A. Capria, S. Pinna, D. Onori, C. Porzi, M. Scaffardi, A. Malacarne, V. Vercesi, E. Lazzeri, and A. Bogoni, Nature **507**, 341 (2014).
9. K. Goda and B. Jalali, Nat. Photon. **7**, 102 (2013).
10. C. Wang and J. Yao, IEEE Trans. Microwave Theory Tech. **61**, 4275 (2013).
11. W. Zou, H. Zhang, X. Long, S. Zhang, Y. Cui, and J. Chen, Sci. Rep. **6**, 19786 (2016).
12. Q. Guo, M. Chen, Y. Liang, H. Chen, S. Yang, and S. Xie, Chin. Opt. Lett. **15**, 010012 (2017).
13. F. Zhang, Q. Guo, Y. Zhang, Y. Yao, P. Zhou, D. Zhu, and S. Pan, Chin. Opt. Lett. **15**, 112801 (2017).
14. G. Yang, W. Zou, X. Li, and J. Chen, Opt. Express, **23**, 2174 (2015).
15. G. Yang, W. Zou, L. Yu, K. Wu, and J. Chen, Opt. Express, **24**, 24061 (2016).
16. H. Zhang, W. Zou, G. Yang, and J. Chen, Chin. Opt. Lett. **14**, 030602 (2016).
17. I. W. Selesnick, Signal **10**, 1 (2009).
18. Keysight Technologies, "M8195A 65 GSa/s arbitrary waveform generator and M8197A multi-channel synchronization module - data sheet,"http://literature.cdn.keysight.com/litweb/pdf/5992-0014EN.pdf (2016).